OPEN ACCESS

The Role of Cu-Based Intermetallic on the Direct Growth of a ZnAl LDH Film on AA2024

View the article online for updates and enhancements.

The Role of Cu-Based Intermetallic on the Direct Growth of a ZnAl LDH Film on AA2024

A. C. Bouali,[1,z] M. Serdechnova,[1] K. A. Yasakau,[2] A. Lutz,[3] G. Wiese,[1] H. Terryn,[3] M. G. S. Ferreira,[2] and M. L. Zheludkevich[1,4]

[1]*Institute of Surface Science, Helmholtz-Zentrum Hereon, Max-Planck-Straße 1, 21502 Geesthacht, Germany*
[2]*CICECO—Aveiro institute of materials, Dep. Materials and Ceramic Engineering, University of Aveiro, 3810-193 Aveiro, Portugal*
[3]*Research Group Electrochemical and Surface Engineering, Vrije Universiteit Brussel, Pleinlaan 2, Etterbeek, Brussels 1050, Belgium*
[4]*Faculty of Engineering, Kiel University, Kaiserstraße 2, Kiel 24143, Germany*

The direct ZnAl layered double hydroxide growth on AA2024 is a fast-occurring reaction, yet is characterized by an inhomogeneous film thickness. It has been shown that at the periphery of Cu-rich intermetallic, the flakes tend to be larger and denser. A combination of in situ and ex situ measurements were used to monitor the changes in the layered double hydroxide film grown on the regions of intermetallics. Immediately after immersion, an activation of the intermetallic phases is observed due to the dealloying process with an almost immediate film growth. Dealloying is followed by trenching of the adjacent Al matrix leading to an excessive production of large and dense layered double hydroxide flakes at the periphery of the intermetallic. However, the scanning electron microscopy cross-section images revealed that the trenching process leads to defects in the area surrounding the intermetallic. This could weaken the corrosion resistance performance of the layered double hydroxide conversion coating and lead to adhesion failure of consecutive polymer coatings. Nevertheless, this work highlights a few advantages and drawbacks of the layered double hydroxide conversion coatings and pathways to its potential optimization and improvement.

Aluminum alloys are extensively used in aerospace and automobile industry, owing to their countless properties which could be easily engineered to meet the requirement of specific applications.[1–3] Aluminum alloy 2024 (AA2024), with copper as the primary alloying element is largely used for aircraft manufacturing industry due to its lightweight, strength and high damage tolerance properties. However, AA2024 has a relatively complex microstructure and contains intermetallic (IMC) phases that makes it susceptible to corrosion.[4–7] Therefore, surface treatments and protective coatings are necessary for its use in specific applications.[8–11]

Conversion coatings serve several purposes some of which are the function of barrier protection, active corrosion protection but also adhesion promotors for further coating and paint applications. Chromate conversion coatings (CCC) used to be the standard most efficient corrosion protective system for automotive and aircraft industries before they were banned some years ago due to their toxicity.[12,13]

Chromate conversion coatings are applied on Al alloys by a process that allows the generation of polymer chains composed of covalent Cr(VI)–O–Cr(III) bonds. The latter covalent bonds serve to store the active Cr(VI) species and release them upon the appearance of corrosion activity.[14,15] However, in spite of their remarkable corrosion protection capabilities, they still failed to provide a long-term corrosion resistance for Al alloys with a high percentage of copper (4 to 5%). In a study of McGovern et al.,[16] it was shown that during the CCC formation, Cu-rich IMCs such as AlCuMg and Al_2CuMg, may obstruct the reduction of Cr(VI) to Cr(III) that permits the establishment of the mixed metal Cr(III)-Cr(VI) oxide that is the backbone of the CCC corrosion protective properties; the CCC film formation is slowed down around the Cu-rich IMCs. This finding was confirmed in another study where a thinner CCC was detected in the area of Cu-rich IMC in comparison to the rest of the matrix; and it was associated with the absorption of ferricyanide, that were used as accelerators, on these IMCs blocking the CCC growth

and a deficiency of Al^{3+} cations in the IMC which are an essential part of the CCC formation mechanism.[17]

The influence of Cu-rich IMC on the mechanism of conversion coatings formation was also reported on the recent alternatives to CCC. For instance, a few investigations of the mechanism of trivalent chromium process (TCP) growth on Cu-containing Al alloys, showed that the precipitation is initiated around S-phases induced by an increase of the local pH.[18,19] However, a thicker TCP layer is not always linked with better corrosion resistance. For Al alloys with higher Cu-coverage, the TCP appeared to be thicker but presented low corrosion resistance properties.[20] P. Campestrini et al.[21] revealed that the mechanism of formation of cerium-based conversion coatings (CeCC) takes place through the deposition of cerium oxide particles that are subsequently connected to form a thin conversion layer at the surface of AA2024.

Similar to the TCP formation, the nucleation of the cerate film is driven by the presence of Cu-rich particles at the surface. Moreover, the effect of the Cu particles is highly dependent on their distribution around the surface and content in the Al alloy substrate.[21] The influence of the size and distribution of Cu IMCs on the formation of CeCC was further highlighted by S. Sainis et al.[22] Accordingly, at short immersion times a preferential thick deposition of CeCC takes place only on the highly active Cu-rich IMCs whereas a thin CeCC layer is observed on the rest of the surface. In addition, the CeCC deposition on an isolated Cu rich IMC appears to disperse in an equal manner along every direction whereas in a network of IMCs (e.g., Cu-rich IMC connected to Si and Fe rich particles), the deposition process is hindered and a lower extent of deposition is observed.[22] Zr/Ti conversion coatings also appear thicker close to the Cu-rich IMC.[23,24] The oxygen reduction reaction, taking place at the IMCs, induces the fast hydrolysis of metal hexafluoride precursors (ZrF_6^{2-} and TiF_6^{2-}) and the precipitation of the respective oxides. In a different study involving a Zr/Zn conversion coating, L. Li et al. managed to capture images of an enriched Zr precipitation over dealloyed Cu-rich particles which indicated that the coating does form on the IMCs.[25]

Layered double hydroxide (LDH) is an emerging functional material that demonstrated attractive active corrosion protection

[z]E-mail: anissabouali05@gmail.com

properties.[26–32] LDH nanocontainers can be exploited through two different pathways as pigments or as conversion coatings. In both scenarios, corrosion inhibitors can be intercalated in the LDH galleries and released upon specific triggers. LDH conversion coatings can be produced directly on Al alloys through several chemical/electrochemical processes, with the co-precipitation method being the most common. Overall, the mechanism of the LDH growth tends to be complex. A number of studies have reported that the LDH film growth undergoes different stages, which are mainly characterized by the dissolution of the native oxide layer, formation of an intermediate Al hydroxide layer followed by the appearance of the first LDH flakes and thickening overtime to convert into a dense and thick LDH conversion layer.[33–35]

A.C. Bouali et al. confirmed the above findings, but a few additional facts were uncovered.[36] The intermediate layer is believed to be a pseudo-boehmite like in nature rather than an Al hydroxide gel-like layer. It was proposed that the increase of the local pH leads to the partial dissolution of this pseudo-boehmite intermediate layer that contributes to the formation of the LDH flakes at the surface. More importantly, the kinetics of the LDH growth appear to be governed by a 2D diffusion-controlled reaction with zero nucleation rate.[36] Furthermore, the possible Cu-redeposition on some area of the Al matrix and its role on the overall mechanism of LDH growth were discussed. Indeed, it has been reported that on areas where Cu-rich IMCs were present, LDH tends to grow in form of islands with larger flakes in comparison to the rest of the matrix.[27,37,38] This effect was attributed to the fast dissolution of the surrounding Al matrix driven by the galvanic effect triggered by the more noble element (Cu) compounds.

In the present work, a closer look to the reactions happening at the area on the Cu-rich IMC during LDH growth was taken. The AA2024 used was not subject to any surface pre-treatment in order to reduce any additional statistical parameter that could also influence the mechanism.

A combination of different methodologies was used to explain what happens at the area of the IMC, the parameters that could play a relevant role on the film formation at this zone and their consequences in the stability of the overall formed LDH film.

Experimental

Materials.— *Chemicals.*—The synthesis of LDH growth was achieved using the following reagents: zinc nitrate hexahydrate $(Zn(NO_3)_2 \cdot 6H_2O$, >99%, CarlRoth, Germany), ammonium nitrate $(NH_4NO_3$, >98.5%, Bernd Kraft, Germany), ammonia solution $(NH_3 \cdot H_2O$, 25%, Merck KGaA, Germany) and deionized (DI) water.

Substrate.—The AA2024-T3 used in the current work were purchased from Aircraft Materials (UK) and has the following nominal composition in wt%: 90.7–94.7 Al, 3.8–4.9 Cu, 0.5 Fe, 0.1 Cr, 1.2–1.8 Mg, 0.3–0.9 Mn, 0.5 Si, 0.15 Ti, 0.25 Zn and 0.15 others. The specimens were cut into squares of 10 mm × 10 mm. For simplification, the designation of AA2024 will be used instead of AA2024-T3, in the rest of the manuscript.

Methods.— *LDH film growth.*—The LDH conversion coatings were produced by co-precipitation method following the same procedure described in.[27,37,39,40] Briefly, the AA2024 specimens were immersed in a synthesis bath containing a mixture of 0.1 M $Zn(NO_3)_2$ and 0.6 M NH_4NO_3. The pH of the bath was of 6.5, obtained after adjusting with 1 wt% ammonia solution. The synthesis process took place at 95 °C and the immersion time varied from 1 to 30 min, depending of the investigation method.

Characterization.— *Atomic force microscopy (AFM)/Scanning Kelvin probe force microscopy (SKPFM) measurements.*—The AFM/SKPFM measurements were performed using the same procedure reported in a previous work.[36] Briefly, the AFM/SKPFM investigation was carried out using a Digital Instruments

NanoScope III Microscope (former Veeco instruments) equipped with an Extender™ Electronic Module. The interleave mode with two pass scans was selected for the SKPFM measurements. The first scan measured the surface topography, while the second scan assessed the Volta potential difference (VPD) between the AA2024 surface and the AFM tip using the nulling technique. All VPD measurements were performed at a lift height of 100 nm with applied AC voltage of 5 V RMS between the tip and the AA2024 sample to cause electrostatically induced oscillations. The output VPD was inverted to align with the standard electrochemical scale and the more negative values represented electrochemically active sites, while the more positive potentials represented electrochemically more noble sites.

The AFM/SKPFM maps were acquired using n-doped silicon probes (Budget Sensors) covered with Pt. The size of the maps was 40 × 40 μm (256 × 256 points). The topography maps were flattened to improve the readability and the reported VPD values were referenced vs the Pt probe. The potential of the probe was checked vs a polished Ni surface and the deviation of potential was in the range of 30 mV. Moreover, at least three different zones on each sample were analyzed to attest for variation of potential.

Focus ion beam (FIB)/Scanning electron microscopie (SEM) analysis.—The SEM top view and FIB cross-section examination of the LDH films was performed using a Tescan Lyra 3 set-up (TESCAN GmbH, Dortmund, Germany) equipped with an energy dispersive X-ray spectrometer (EDX) Ultim 100 SDD detector (Oxford Instruments, High Wycombe, UK). The data was assessed using the Aztec software from Oxford Instruments.

The SEM analysis was conducted using the secondary electron (SE) mode and an accelerating voltage of 2 kV was used when working with LDH films. This is in order to avoid the issue with charge accumulation. However, on non-LDH surface a voltage of 20 kV was used.

The FIB cross-sections of the LDH lamella were obtained using a Ga driven Cobra FIB attached to the TESCAN set-up. A Pt layer was deposited on the LDH films using a gas injector system (GIS).

Confocal Raman spectroscopy.—A LabRAM HR Evolution confocal Raman spectrometer (Horiba Scientific, France) was used to analyse the LDH treated AA2024. A green 532 nm wavelength laser at 50% intensity (approx. 7.5 mW cm^{-2}) was used to record the Raman spectra and a built-in microscope with a 100×objective for Laser spot positioning and taking the optical images.

The instrument was operated with the standard LabSpec 6.2 software, by Horiba Scientific, which also allowed for data treatment like spike removal and background correction of each spectrum.

In situ atomic emission spectroelectrochemistry (AESEC).— AESEC measurements were performed using an AMETEK ICP spectrometer (AMETEK, USA) connected to a Gamry Interface 1010E potentiostat (Gamry, USA). A similar AESEC set-up described in a previous study[37] was used for the current investigation. Briefly, the set-up consists of an in situ cell that permits the electrochemical evaluation of the testing material as well as a direct analysis of the elements which are released to the electrolyte.

A Spectra/Por® 4 RC dialysis membrane (electrically but not ion conductive) is separating the cell to prevent the loss of released ions during the electrochemical measurements. Using a peristaltic pump, the electrolyte with the dissolved species from the specimen is continuously fed into the plasma, where the emission lines of the main components are analyzed and compared with the electrochemical data, obtained with the Gamry potentiostat.

The measurements were performed at 95 °C in the electrolyte precursor to LDH growth. The exposed area of the AA2024 sample was 0.5 cm^2 (d = 8 mm). The electrolyte volume was of approx. 0.5 cm^3 (flowrate ∼ 2 ml min^{-1}). During the LDH formation and electrochemical measurements, the electrolyte was continuously renewed with a flow rate ∼ of ca. 2 ml min^{-1}).

For all above investigations, the AA2024 test samples were abraded with SiC abrasive papers till 2500 grit size. The only exception was for the AFM/SKPFM measurements where they were abraded then polished with diamond pastes down to 1 micron and then finishing with 100 nm alumina DI water-based suspension.

Results

Ex situ AFM/SKPFM measurements.—Figure 1 presents the topography and Volta potential maps of AA2024 surface before and after different immersion times (i.e., 0, 1, 3, 6 and 15 min) in the LDH synthesis bath. The maps before treatment essentially show two big IMCs, marked by white arrows, that are barely visible on the topography map, but having a brighter contrast in the Volta potential map with more positive VPD vs the aluminium matrix (Fig. 1). Various small dispersoids and constituents indicated with green arrows, are visible only on the VPD map of the as polished aluminium (Fig. 1a "0 min"). These compounds have more positive corrosion potential than pure aluminium and show contrast on the Volta potential maps.[5]

Upon just a short immersion in the electrolyte, there are visible changes in topography which are caused by precipitation/growth of a conversion film on the surface. Much more growth occurs at the areas of large IMCs (Fig. 1 IMC 1). At the beginning of immersion, more precipitates formed at the borders of S-phase particle, IMC 1 (Figs. 1e–1f "3 min").

The topography profiles (Fig. 2a), which are indicated by the lines in each map from Fig. 1, demonstrate two main elevations/peaks emerging after immersion and increasing in height overtime. They clearly correspond to the LDH flakes situated at the edges of the IMC.

Interestingly, the VPD contrast becomes more negative compared to the matrix at the places of IMC compared with the matrix after immersion which leads to the assumption that the conversion product layer or surface oxide film contributes to the measured VPD. The dark area becomes much larger at longer immersion times, in comparison to the initial dimensions of the IMCs (see VPD map at 0 min immersion Fig. 1). It appears that the precipitates on the IMCs have different properties (surface chemistry, composition etc.) which affect the measurements as it can be seen on the VPD map taken after 15 min immersion (Fig. 1) and on the topography profiles (Fig. 2a).

Changes in passive film composition at the metal surface or distribution of copper at the surface may effectively contribute to the measured potential as it has been suggested in our previous publication.[36] Average VPD levels show rapid increase of VPD immediately after 1 min of immersion in the synthesis solution with the VPD level being stable up to 6 min of immersion reaching about −0.45 V vs Pt tip (Fig. 2b).

A further immersion up to 15 min caused an increase of VPD to approx. −0.36 V vs Pt tip. This increase may be accompanied with some chemical changes in the conversion layer and passive film. However, it is not clear how the changes in the passive film and properties of the conversion layer contribute to the measured VPD. Moreover, there is a significant difference in reactivity of IMC 2 in comparison to IMC 1.

For the reference, the VPD potential of Cu was measured (polished with diamond pastes and cleaned in 2-propanol) and is about −0.30 +/− 0.03 V vs Pt tip. The VPD measured on the alloy after 15 min of immersion, is just slightly lower than that of Cu (Fig. 2b). However, the measured Volta potential seems to be attributed to the properties of precipitates on the surface rather than properties of the underlying IMCs as seen on the profiles across the IMC "1" after 15 min (Fig. 2). Most of the changes reported in Fig. 2 concern the IMC marked "1" (Fig. 1 "0 min"), whereas a very different behaviour, less pronounced, can be seen for IMC "2".

In order to clarify the contribution of corrosion product to VPD, an additional experiment was performed in the same immersion setup but using pure DI water. The surface of the polished AA2024
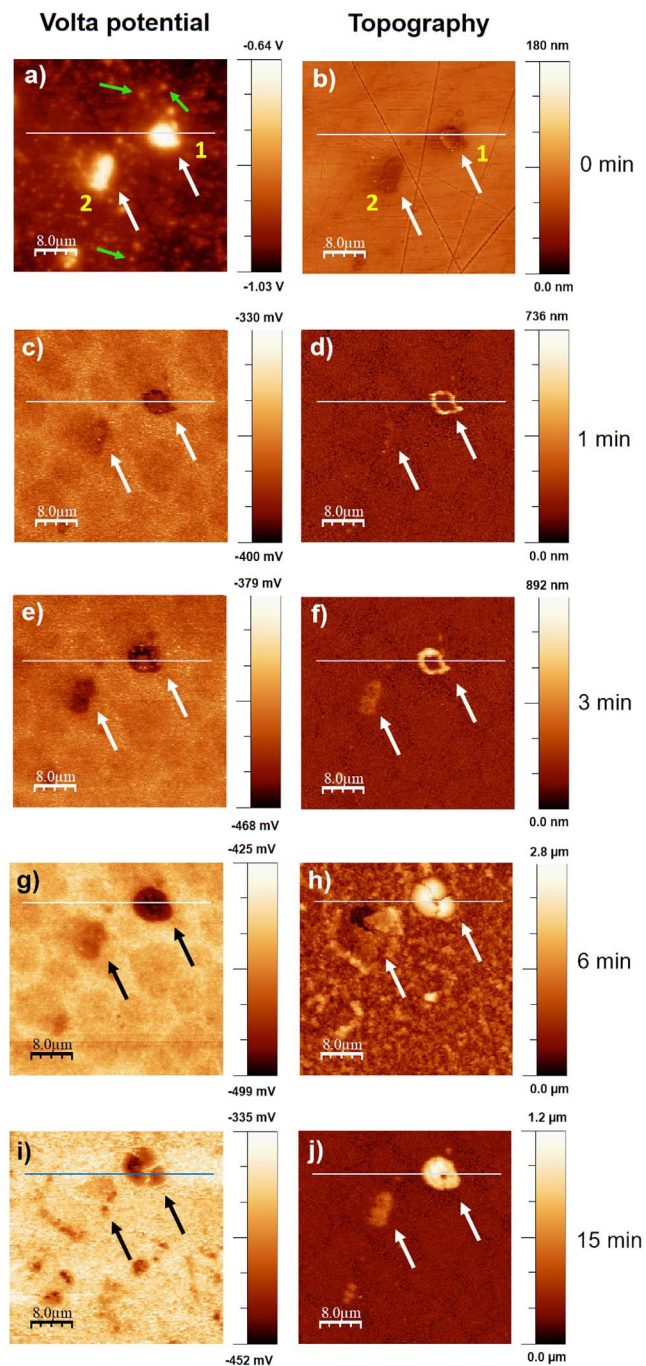

Figure 1. Topography (left) and VPD (right) changes before and after different immersion times in the LDH synthesis bath.

shows the same features which were observed in Fig. 1. For instance, large IMCs (highlighted by arrows since they are barely visible on topography maps), various dispersoids and constituents that have more positive VPD vs the aluminium matrix (Figs. 3a and 3b). Upon immersion in DI water, the IMCs undergone partial dealloying and the topography level of IMCs decreased compared with that of the matrix (Fig. 3g). Indeed, after 6 min immersion in DI (Fig. 3g red line) it can be seen that the topography level decreases (to about -500 nm vs. the matrix) at the area of the intermetallic with a much-pronounced decline at the border of the IMC (marked by two side dents in the curve). At 15 min (Fig. 3g green profile), the decrease is relatively homogeneous along the IMC.

Moreover, the average VPD value increased on the entire surface (Fig. 3h). However, a larger increase occurred around the IMCs
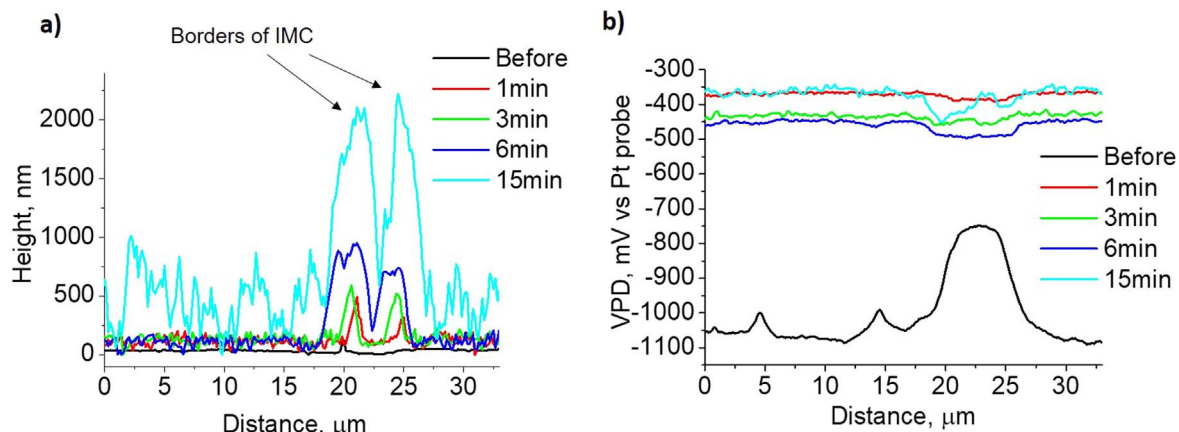
Figure 2. Topography (a) and VPD (b) changes along the profiles shown in Fig. 2 (straight lines) of AA2024 surface before and after different immersion times in the LDH synthesis bath.

(Figs. 3d, 3h "6 min"). Such VPD increase may be associated with the well-known Cu redeposition process around intermetallic.[34,36,41,42] A lower VPD measured at the top of IMC may be related to lack of copper after the dealloying of S-phase in pure water during the first 6 min of immersion, but also to the formation of corrosion products on S-phase that can affect the VPD measurements. This decrease is also observed for small Cu-based particles, as it can be noted with the small drop at approx. 5 μm (see arrow in Fig. 3h). At longer immersion time, the VPD values at the matrix and IMC continued to increase but the dealloying did not go further (Figs. 3e, 3h "15 min"). There is a discrepancy in terms of the VPD values of the AA2024 surfaces when the two experiments are compared (Figs. 2b and 3h). First, corrosion precipitates apparently slow down the dealloying of S-phases at the very beginning of immersion in the LDH synthesis bath unlike for the DI water bath.

Moreover, the LDH layer contributes to the VPD so there can be only semi quantitative comparison with the Volta potential level of pure copper. Still, when the pure aluminium is exposed to the boiling DI water the VPD values did not increase in spite of the precipitation of boehmite phase on the surface.[43] This essentially points out that the copper redeposition process is important for the growth of LDH on the AA2024 surface and the copper-containing IMCs are necessary to increase the pH at the surface.

SEM/EDX analysis.—Figure 4 displays top-view SEM images of the AA2024 surface samples with different immersion times, in the LDH synthesis bath. Each image belongs to a different IMC area from a different AA2024 sample that was removed at a specific period of time (0.5, 1, 3, 6, 10 and 15 min).

After only 0.5 min, a thin layer of LDH can already be seen over the surface. The LDH film is overall homogeneous, except for the zones of IMCs where massive clusters of LDH flakes are formed. With prolonged immersion times, the LDH film continues to densify and the flakes around the IMC continue to increase in size . Looking closely at the images after 0.5, 1, 3, 10 and 15 min, the LDH flakes around the intermetallic seem to form preferentially at the edges of the IMC. However, a fine layer of LDH flakes is also formed directly above the IMC. In some cases, the larger LDH flakes develop an interconnection and cover the entirety of the IMC area (Fig. 4 "6 min").

The elemental composition of the underlying areas of these LDH islands was analysed and disclosed in Fig. 5.

Figures 5a and 5b display the EDX maps (Al, Zn, Cu, N, O and Mg) after 0.5 min and 15 min of LDH growth, respectively, whereas Fig. 5c represents the superposition of the Al, Zn and Cu maps for the sample after 0.5 min immersion. The additional EDX maps at 0, 1, 3, 6, 10 min are provided in the supporting information (Fig. S1 (available online at stacks.iop.org/JES/169/081501/mmedia)).

An unevenness of the elemental distribution over the surface can be noticed in both Figs. 5a and 5b. Although the dark contrast is depicted on the Al maps on the zones of the LDH islands, this does not mean that Al is absent in the LDH flakes composition. This is due to the fact that less X-ray are emitted from the Al in the flakes in comparison to the rest of the AA2024 surface. Conversely, elements such as Zn, O and N are more concentrated on these LDH islands due to the difference in thickness in comparison with the thin LDH layer formed on the rest of the AA2024 surface.[38]

Another important observation is the presence of Cu below the LDH islands. As a matter of fact, when performing EDX maps on a larger LDH coated surface area, Cu was uncovered at every of these LDH flower like zones (Fig. S2). This clearly emphasizes the role of Cu-rich IMCs in the mechanism driving the formation of these voluminous LDH islands.

Mg was also detected on most of these zones (Figs. 5a, 5b, S1–2) which suggests that the IMCs are S-phase (Al$_2$CuMg) compounds. Outside the IMCs, Mg was not observed. The larger LDH flakes surrounding the IMC are mainly composed of Al, Zn, O and N.

The manner, in which the elements constituting the LDH flakes (e.g., Zn, N and O) are distributed around the edges of the Cu particles together with the size of the LDH flakes, implies that the kinetics of the LDH formation on these specific regions is faster than in the rest of the matrix. In order to verify this hypothesis, a closer examination of the area below the LDH islands was performed by means of cross-section images followed by EDX analysis. The results are depicted in Figs. 6 and 7, with Fig. 6 representing the sample after 0.5 min LDH synthesis and Fig. 7 after 15 min. The dashed lines across the EDX elemental maps were added for clarity, to indicate the lower part of the IMC and the LDH flakes at the interface.

In Fig. 6, the EDX analysis captures the cross-section of two IMC particles close to each other, after 0.5 min immersion. A similar deduction can be made with the EDX cross-section maps in terms of the irregularities in the elemental distribution. Elements such as Zn, N, O are detected on the area of the LDH flakes whereas Cu and Mg can be seen on the cross-section side of the maps as part of the embedded IMC composition. The black halo observed with the Al EDX map is due to an artifact caused by the geometry setup of local cross-sections. The sample and the EDS were tilted in different angles. With the used setup a darker area in the direction of the rotation of the detector at light energies is observed if the sample surface is topographically higher or has higher density. This could potentially influence the interpretation of the results as it lowers the visibility of concentration differences.

Enlarged cross-section images for the sample after 15 min LDH synthesis are displayed in Fig. 7a. From the micrographs, it can be seen that a dissolution of the alloy matrix during the LDH synthesis
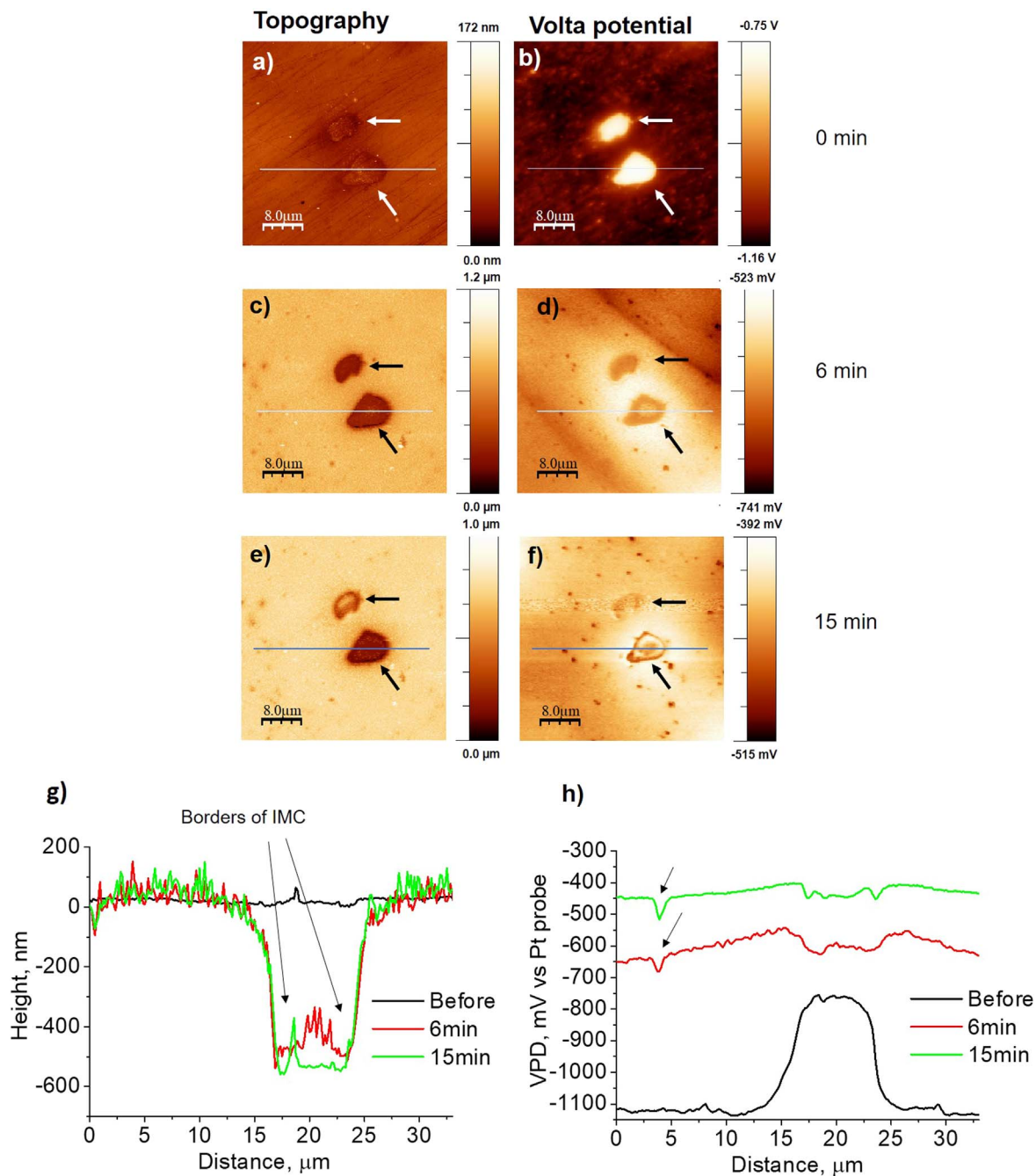
Figure 3. Topography (a), (c), (e) and VPD (b), (d), (f) changes of AA2024 surface before and after different immersion times in 95 °C DI water; the corresponding topography (g) and VPD (h) profiles as indicated with a line in the VPD and topography maps (a)–(f).

takes place on the edges of the S-phase particle. Indeed, a presence of some sort of voids/crevasses on the corners of the IMC which shows up in dark on the SEM micrograph are rather obvious. This is basically a consequence of the Al anodic dissolution induced by the micro-galvanic coupling with the nobler Cu-rich particle.[5] The accelerated dissolution of the Al matrix adjacent to the Cu IMC promotes a faster rate of ZnAl LDH formation which leads to the generation of larger LDH flakes on the areas of the voids and their efficient coverage.

Next to the dissolution of the Al matrix, a thin film is formed above the S-phase particle below the LDH conversion layer (Fig. 7a). The EDX maps in Fig. 7b indicate that this film is mainly rich in Cu and O which suggest that it could be a layer of Cu oxide. However, despite the presence of a Cu oxide layer, a continuous and

defect-free LDH layer can be observed above the Cu-rich IMC. In other words, there is undeniably still access to Al that would permit the formation of the LDH building blocks.

For the purpose of clarification, the cross-section images shown in this section were not repeated for the case of 15 min immersion and repeated once for the 0.5 immersion time.

Confocal Raman spectroscopy.—In an attempt to obtain more information on the LDH growth around the IMCs, ex situ Confocal Raman spectroscopy was used to monitor the LDH growth at different periods of immersion times (0, 1, 3, 6, 10, 15 min) (Fig. 8). Images were taken before every measurement (Fig. 8a) and Raman spectra were obtained by targeting two main points; (1) on the matrix (just outside the IMC) and (2) on the IMC, as
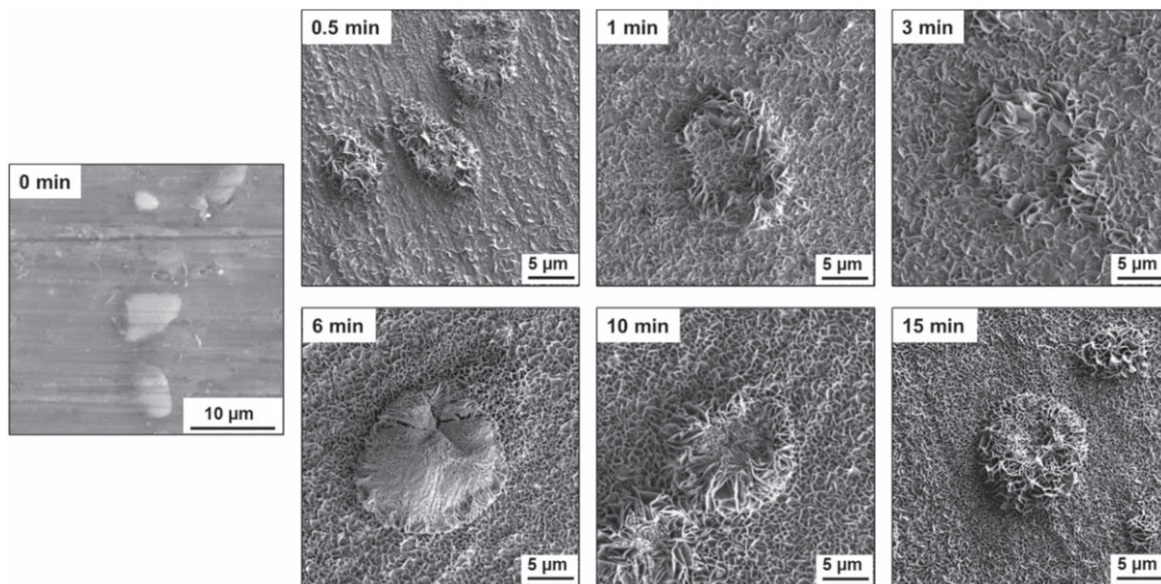
Figure 4. SEM micrographs of IMC areas exposed to different immersion times in an LDH synthesis bath.

represented in Fig. 8a "0 min." The respective spectra are labelled in Fig. 8 as **b** and **c**. The changes in the spectra are registered from t = 0 min to t = 15 min (see arrow on the right side of Fig. 8c).

Starting with the Raman data obtained on an area of the matrix, no Raman bands associated with LDH were registered at 0 min and 1 min (Fig. 8b). After 3 min of LDH growth, 4 different Raman bands can be noticed in the region between 400 and 1200 cm^{-1}. The band around 495 cm^{-1} was previously ascribed to an OH group strongly coordinated to Zn, whereas the band at 562 cm^{-1} is associated to an Al–OH translation.[44] The Raman bands at 714 cm^{-1} and 1050 cm^{-1} emerging after 6 min and 3 min, respectively, can be assigned to the asymmetric bending and symmetric stretching vibrations of NO$_3^-$.[45,46] The assignment of the NO$_3^-$ vibration is not straightforward, some studies consider the 1050 cm^{-1} to be associated to free NO$_3^-$ non-bonded to the hydroxide layers.[44,47,48] However, in another study, the NO$_3^-$ vibration was paired with a Raman band close to 690 cm^{-1}.[45] In the current circumstance, a Raman band at 714 cm^{-1} was detected and can be linked to an NO$_3^-$ vibration in hydrotalcite.[45,46,49] Therefore, according to these results and the literature, it is reasonable to assign the Raman bands to an NO$_3^-$ vibration in the LDH galleries.

The region between 1300 cm^{-1}–1700 cm^{-1} seems to be marked by an overlapping of several bands (Fig. 8b). From the spectra at 3, 6 and 10 min, three peaks can be identified; ~1330, ~1380 and 1600 cm^{-1}. It was not possible to explicitly assign these bands from the literature. However, the literature often associates these bands to the G and D bands of carbon. They are possibly an artifact from the burning caused by the beam.[49] For comparison, a Raman measurement was performed on an LDH slurry and some of the Raman bands found on LDH conversion film on AA2024 could be identified as well on the LDH slurry. The spectrum is illustrated in Fig. S3 of the supplementary information.

The Raman spectra from the IMC (Fig. 8c) shows a similar pattern of Raman bands as the matrix, with a few exceptions. For instance, the Raman band at approximately 300 cm^{-1} is present from 0 min and its signal intensifies till 10 min and disappeared at 15 min. In line with the Raman data obtained in the literature on copper-based substrates, this band can be ascribed to one of the CuO vibration modes.[50–54] The increase of the intensity and the sharpness of the peak was justified by a possible decrease in the grain size of the CuO particles.[52] The absence of the Raman band associated to CuO at 15 min can be explained by the strong coverage of the area

with LDH flakes. This is reflected at the cross-section images taken after 0.5 and 15 min LDH synthesis (Figs. 6 and 7). The intermetallic phase as well as the supposed formed Cu oxide layer are no longer accessible for detection. A similar behaviour was reported in a study, where an in situ XRD monitoring of LDH growth on an AA2024 substrate was done.[36]

Between approx. 400 and 700 cm^{-1}, a broad band is observed after 1− and 3 min immersion. Here, a superposition of several bands associated to the presence of various species is probable. Their assignment cannot be resolved, since during the first minutes of immersion there might be a simultaneous presence of several Cu complexes[55] as well as the species taking part in the LDH formation. After 6 min immersion, the Raman bands appear more defined and splitted. For instance, at 6 min, the bands at 495 cm^{-1} and 562 cm^{-1} previously observed on the matrix, can be distinguished and have the same assignments. A small peak at approx. 615 cm^{-1} could also be noted. According to some studies performed on Cu oxide compounds, this band corresponds to an additional CuO Raman active mode.[53–56]

The Raman band at 714 cm^{-1} is absent, instead a peak at 724 cm^{-1} is seen after 6 min LDH synthesis (Fig. 8c). The later Raman band was also linked to the NO$_3^-$ asymmetric bending.[48] In a study from J.T. Kloprogge et al., it was stated that changes in the interactions between the nitrates and the interlayer water or the hydroxide layers may lead to a slight shift of the wavenumbers of the nitrate modes which could explain the shift from 714 cm^{-1} to 724 cm^{-1}.[47] A similar explanation can be provided for the shift from 1050 cm^{-1} to 1054 cm^{-1} for the spectra taken after 6 min and 10 min. In a similar context, one study looking into the Raman vibrational spectra of Cu nitrate complexes, identified a prominent nitrate band centred at approx. 722 cm^{-1} which was associated to the Cu(NO$_3$)$^+$ complex.[54] The latter assignment is credible, considering the environment close to the IMC.

However, the spectra at 15 min shows two Raman bands at 1050 cm^{-1} and 1068 cm^{-1}. An enlarged window at those positions, is provided in the supplementary information (Fig. S4). The first Raman band belongs to the NO$_3^-$ vibration mode, while the second most probably to a symmetric stretching mode of CO$_3^{2-}$. The increase of the local pH at the IMC favours the presence of CO$_3^{2-}$ anions which could get effectively intercalated between the LDH layers. All of the bands identified above were summarized with the respective assignments in Table SI.
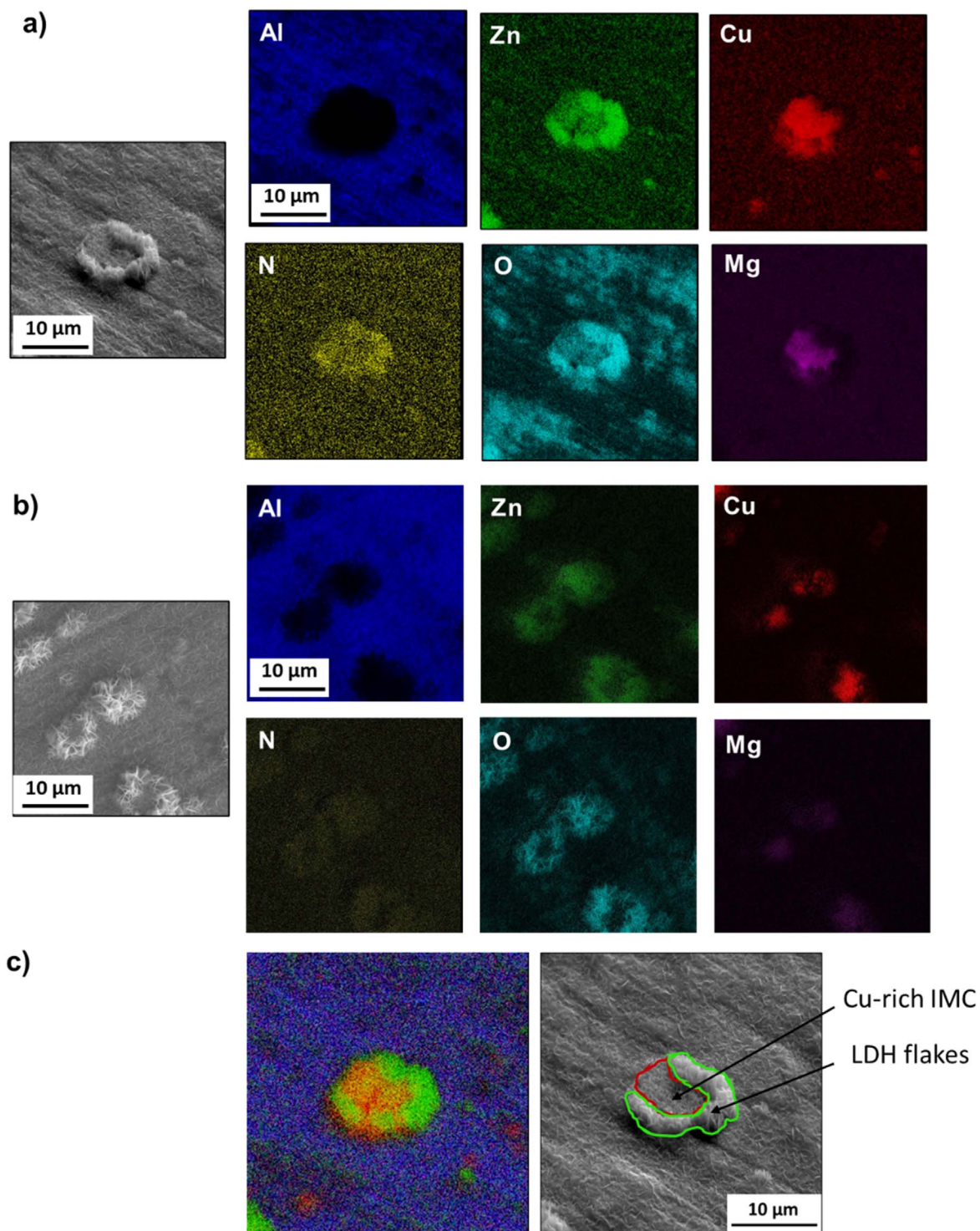
Figure 5. EDX maps of AA2024 surface after 0.5 min (a), 15 min (b) immersion in the LDH synthesis bath and overlapping of the Al, Zn and Cu maps from 0.5 min (c).

Aside from enabling the comparison between LDH formed on the matrix and on the IMCs, confocal Raman spectroscopy was also used to identify changes on the grain boundaries. In Fig. 9, spot measurements were taken in three area: within the grain (Mx-1), IMC and on the grain boundaries (Mx-2). From the images and the spectra (Fig. 9), it is demonstrated that no LDH film is formed on the grain boundaries even after 15 min synthesis.

In situ AESEC measurements.—In order to learn more about the dissolved species during the LDH growth, in situ AESEC measurements were performed. This technique allows to simultaneously assess information on the dissolution rate of selected elements from the AA2024 substrate in a solution containing LDH synthesis precursors while recording any electrochemical changes taking place at the interface.[37,57] The results of the AESEC dissolution profiles of Al, Cu, Fe and Mg together with the recorded OCP values are plotted in Fig. 10.

An evident observation from Fig. 10 is that the dissolution of Cu was quite spontaneous and was observed at the first minutes of immersion. Indeed, between 0 to 500 s, a gradual increase on the
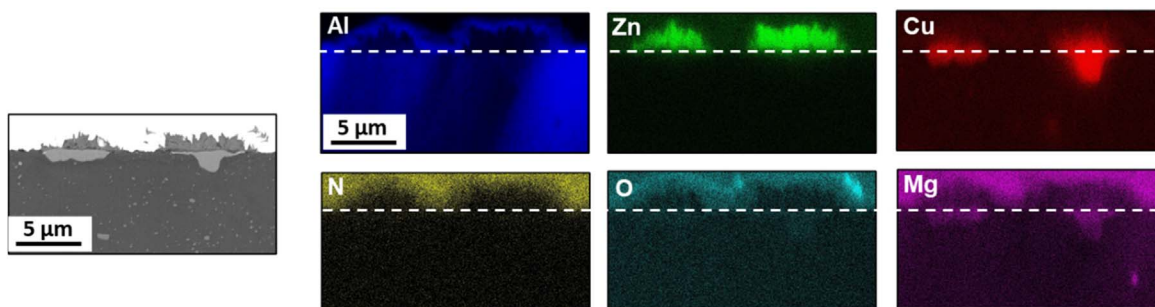
Figure 6. EDX maps of the FIB cross-section IMC areas after 0.5 min immersion on the LDH bath.
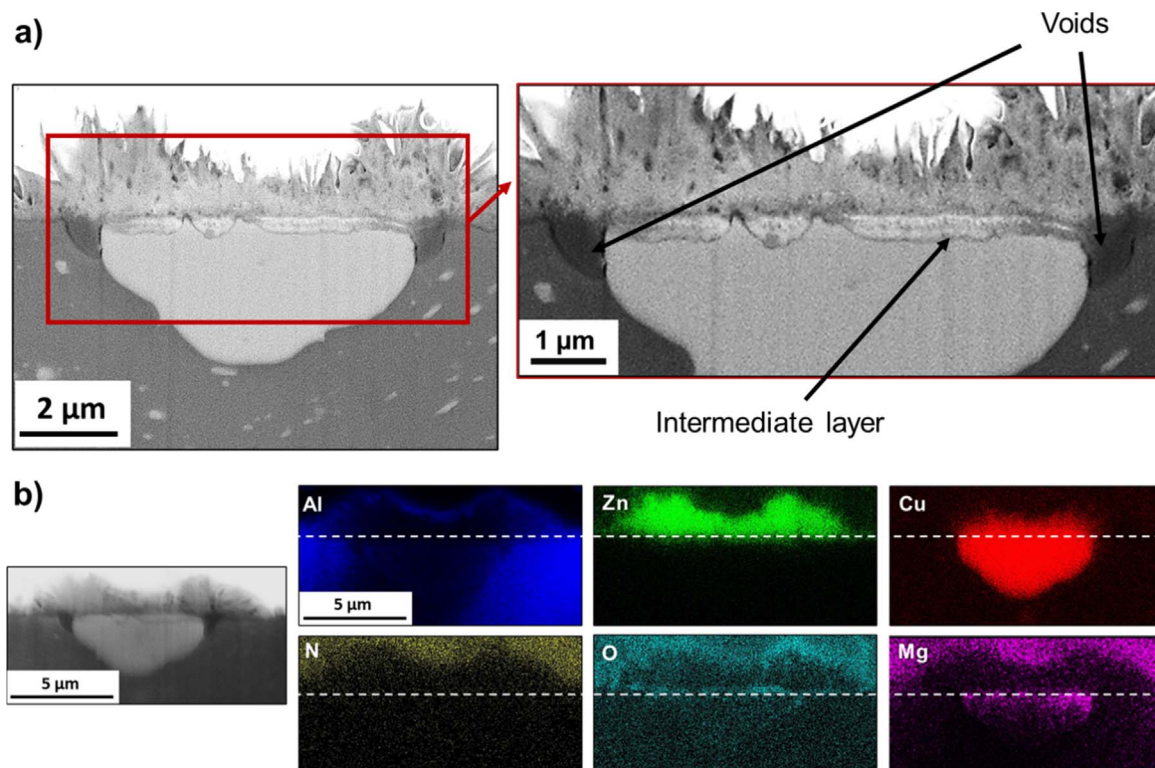

Figure 7. SEM micrograph of the IMC area after 15 min immersion at higher magnification (a) and the corresponding EDX maps (b).

dissolution rate profile of Cu is noted, followed by a slow decrease after reaching a peak at approx. 160 s.

After this first increase in the Cu release at the first minutes of immersion, the process is followed by the appearance of distinctive spikes not only in the dissolution profiles of Cu but also Fe and Mg. One could assume that particles of IMC are being detached (such as Al_2CuMg and Al_7Cu_2Fe) which are then passed into the nebulizer, cyclonic chamber and consequently in plasma. As a matter of illustration, at approx. 390 s (Fig. 10) a strong jump is observed on the Fe and Cu and may correspond to a release from particles rich in Fe and Cu such Al_7Cu_2Fe. In addition to the latter particles, a spike on the Mg profile is also observed, implying the detachment of particles rich in Cu and Mg (e.g. Al_2CuMg) as well. However, a part from the latter mentioned spikes on the Mg dissolution rate, the Mg pattern is not subject to relevant changes overtime. Moreover, some on the Mg spikes are oriented into the negative side of the scale rather than the positive, which could be misleading.

Conversely, the Al profile does not show the presence of Al at the first 500 s of immersion which increases importantly afterwards. At the first seconds of immersion the Al native oxide layer remains stable but gradually undergoes anodic dissolution with an increase of the local pH. Nevertheless, whatever Al is dissolved would be directly consumed on the LDH growth and would not directly be freed into the bulk electrolyte and therefore not fed into the nebulizer.

After some time, the Al consumption is much less substantial either due to the restricted accessibility to the other reactants (Zinc cations) or/and the point of saturation has been reached. This explains the delayed detection of the Al species during AESEC measurements. It should be pointed out that some of the strong spikes after 500 s could also be associated to detachment of LDH flakes from the surface.

Nevertheless, the estimated percentage of the elements mentioned on the latter examples cannot be calculated as there is no guarantee that the elements were completely evaporated into the plasma. The ICP method allows only to detect elements that made it through the diffusion layer and reached the bulk electrolyte. If dissolved elements such as Cu got promptly redeposited on the surface, they cannot be measured by ICP. This could also explain the increase of the Al dissolution rate after some time, since the redeposition of Cu creates localized cathodes that would enhance the anodic dissolution of the Al matrix.

A factor that should be emphasized with the described AESEC measurement is that continuously recirculation/renewing the solution might lead to changes in the concentration of the precursors and
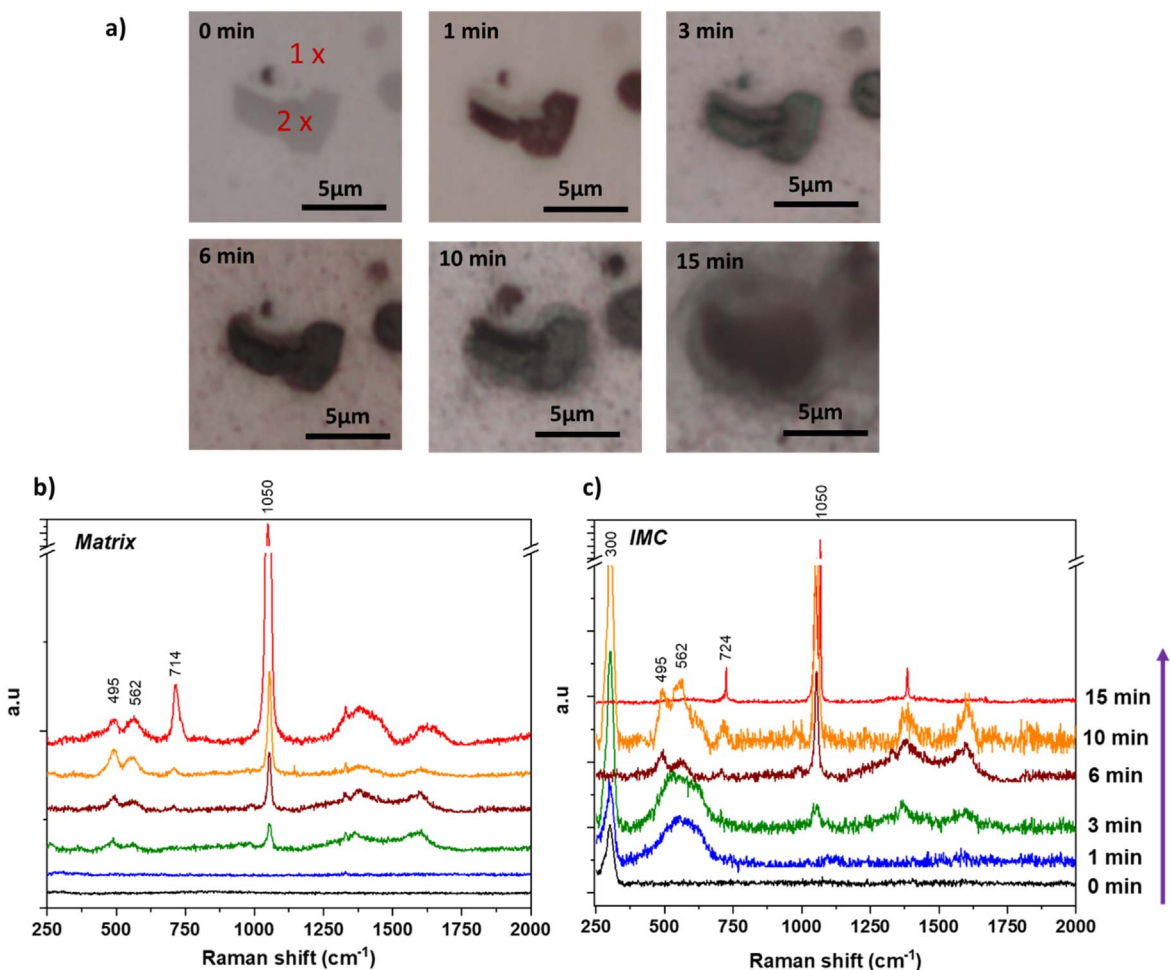
Figure 8. Images of the ex situ Confocal Raman spectroscopy monitoring of the LDH growth (a), with the respective spectra taken on the matrix (outside the IMC) (b) and on a spot in an IMC (c) at different periods of time (0, 1, 3, 6, 10,15 min).

accumulation of Cu rich particle that could increase the cathodic zone. However, not recirculation will lead to inhomogeneous dispersion of the precursors, generation of unwanted products and the perturbation of the synthesis reaction. This is also why in normal synthesis condition, stirring is always required.

Since the data of interest is mainly collected at the first seconds/ minutes of immersion, the impact of recirculating on the interpretation of the results is minimal.

Discussion

The LDH formation on AA2024 is a fast-occurring process, but it is characterized by an inhomogeneous growth along the substrates interface due to the presence of Cu-rich IMCs. The influence of these Cu-based intermetallic was briefly addressed in our previous work,[36] and a clear link has been made between the mechanism of IMC corrosion in AA2024,[4–6,58–61] and the LDH formation reaction.

The AFM/SKPFM results showed a change around the borders of the Cu-rich IMCs within the first minute of immersion which is accompanied with a switch of the IMC VPD to a more negative (anodically active) value in comparison to the matrix. This switch in the OCP has been usually reported for S-phase as the beginning of the anodic dealloying process,[5] but a recent study observed a similar behaviour on most IMCs, where they all were anodically activated during the first seconds of immersion in NaCl solution.[62] However, the corresponding AESEC dissolution profiles show an instant dissolution of Cu, directly after immersion (Fig. 10—first 200 s). At such early

stages, non-faradaic release of Cu particles is possible but dissolution in form of Cu^{2+} seems thermodynamically unlikely.[60,63] It has been reported[60,61] that the S-phase particle dealloying process is more significant and tends to occur in a much shorter time after exposure, in comparison to that of θ-phase particles. It was also suggested that in the case of the S-phase, Cu can be released at a much earlier stage of exposure through the dissolution of detached Cu-clusters from the IMC. Other Cu-based particles present in AA2024 (e.g. Al_7Cu_2Fe, AlCuFeMn) as well as the Cu from the solid solution may also contribute to the release of Cu particles overtime. Some of these particles can be seen on the VPD maps in Fig. 1 ("0 min").

The SEM top-view and SEM/EDX cross-section images (Figs. 4–7) captured at approx. 0.5 and 1 min already show developed LDH flakes specifically at the periphery of the IMCs (Fig. 4). According to the EDX analysis, the IMC seems to match the composition of a S-phase (Al_2CuMg) particle. The dealloying of the S-phase particle involves the preferential dissolution of the less noble elements, Al and Mg, leaving behind a Cu-rich remnant. The latter will act as a cathodic site by inducing oxygen reduction reactions (ORR), increasing the local pH which will in turn cause the disruption of the surrounding Al native oxide layer and the dissolution of the adjacent Al matrix. The latter processes lead to an accumulation of $Al(OH)_4^-$ species in the region which is immediately consumed and used to produce the LDH flakes (Eq. 1) observed in Fig. 4. As demonstrated from the following experiments as well as results presented in a previous work,[36] this process seems to take place very fast and the nucleation of the first
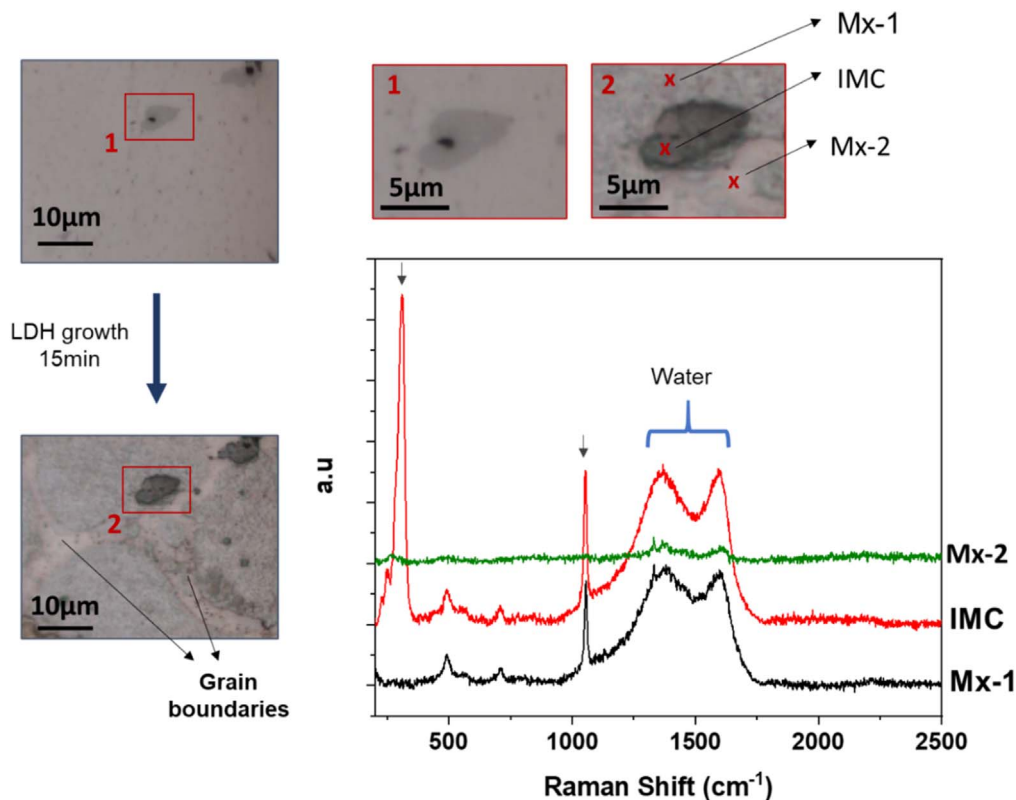
Figure 9. Raman point measurements of three regions around a Cu-rich IMC. Mx refers to matrix and IMC to a spot on the intermetallic.
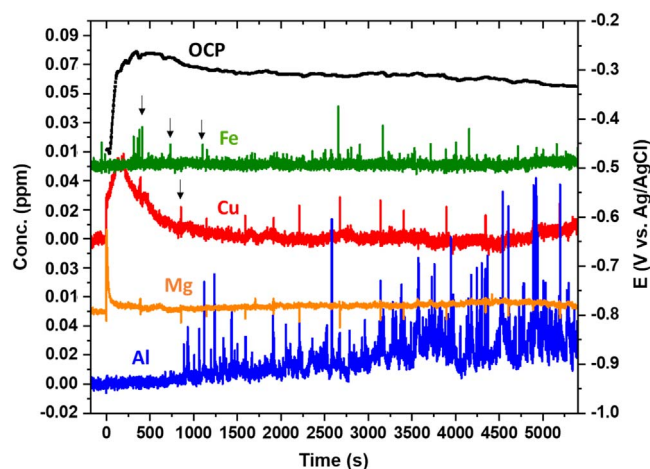

Figure 10. AESEC dissolution profiles (left *y*-axis) of Fe, Cu, Mg and Al plotted together with the OCP evolution (right *x*-axis) during the LDH growth over time.

LDH flakes in quasi-instantaneous at the region of the IMCs. This explains the very low Al signal in the first 500 s of the AESEC dissolution profile.

$$Al(OH)_4^- + Zn(OH)^+/Zn^{2+} + NO_3^- + H_2O \rightarrow LDH - NO_3 \quad [1]$$

The reaction described in Eq. 1 is a simplified overview of a series of reactions that may first involve the deposition of an amorphous $Al(OH)_3$ that will transform to $Al(OH)_4^-$. With regards to the source of Zn, a recent study has shown that ZnO could be formed first at then gradually dissolved to liberate $Zn^{2+}/Zn(OH)^+$ that would recombine with $Al(OH)_4^-$ to form LDH.[64] The detection of ZnO was also suspected in a previous study focusing on the LDH growth

outside the IMC regions.[36] Therefore, both oxide and hydroxide forms can be considered as relevant for the LDH growth.

In the case of Mg, the dissolution profile (Fig. 10) shows some small spikes which overlap with spikes of the Cu and Al dissolution profiles, alluding to a possible release following a dealloying process of IMCs composed of these elements. However, one would expect a much more significant release. Some studies suggested that alkaline environments are unfavourable to Mg dissolution and therefore its release may take longer.[5,65] Another hypothesis is that the released Mg^{2+} is able to slip into the LDH hydroxide layer assembly as a substitute to Zn^{2+}. This is conceivable, although most reported MgAl LDH conversion films were produced in quite different conditions, usually involving high temperatures (i.e., autoclave conditions), longer immersion times and high pH (9–12).[66–68] This latter supposition, cannot be confirmed with EDX as we may be dealing with the inclusion of a few Mg atoms in an LDH hydroxide layer mainly composed of Al and Zn. Despite the fact that MgAl and ZnAl LDH have a different d-basal spacing and lattice parameter "a", it is uncertain whether conventional XRD methods will be able to track the variation, considering the amount of Mg released from the substrate and the Zn precursors in the solution.

Looking into the cross-section of an S-phase particle at an advanced stage of LDH growth, the effect of trenching can clearly be seen on the adjacent Al matrix, as well as a dense LDH coverage just above the dissolved Al matrix (voids). Moreover, a porous layer of Cu oxide is formed on the interface below the LDH flakes. As it has been concluded earlier in the discussion and from Fig. 6 (0.5 min immersion) and Fig. 7, that LDH flakes growth around and above the IMC interface takes place quite fast creating a protective layer that prevents significant dealloying of the IMC particle. Therefore, the formed Cu-oxide porous layer is a result of Cu-particles liberated during the dealloying process. They remain at the interface below the LDH film, as the LDH layer prevents their redistribution. A comparable effect, has been previously observed at the early stages of the corrosion of a θ-phase particle[60] as well as clearly
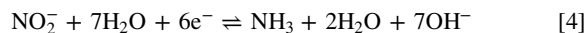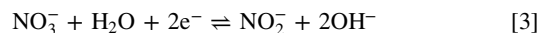
demonstrated in a study about the formation mechanism of LiAl LDH on AA2024.[69] However, the Cu-oxide layer still allows the diffusion of Al(OH)$_4^-$ and the formation of the LDH flakes.

Although, the above-described mechanism was observed on an S-phase particle which is considered a more reactive IMC due to the presence of Mg, a similar LDH growth may be observed on other types of Cu based IMCs. The initiation stage may vary due to the compositional differences of the IMCs in AA2024, yet the local nano-galvanic effect will lead to the fast anodic dissolution of the adjacent matrix contributing to the same enhanced LDH growth.[62]

This study was aimed into understanding the mechanism of ZnAl LDH growth around the IMC, nevertheless the following adverse effects to the mechanism were also picked and need to be addressed: (i) *the voids* (Fig. 7) left on the sides of the IMC as a result of trenching. Indeed, the LDH film formed above the IMC may minimise the effect of dealloying, but it seems that it is not able to compensate the gaps left from the trenching. In other words, the process of LDH growth leads to the creation of pits that can potentially compromise the corrosion resistance and durability of the AA2024 substrate. Aggressive ions such as chlorides may find their way into these gaps and enhance pitting corrosion of the substrate. (ii) *Weak adhesion* to consecutive polymer coating. Some areas may have undergone even further trenching which implies that the IMC is unstable and not strongly connected to the substrate. Hence, they can be easily detached. Moreover, the LDH islands on these IMCs may provide some barrier protection to the voids, but weaken the adhesion of the polymer coating due to the significant inhomogeneous LDH thickness. (iii) Another important drawback of the LDH islands on the IMC, is that they are prone to **osmotic blistering**. This can happen if there is a difference of solute concentration, inducing an osmotic pressure and movement of water from a low concentration region (bulk solution) to a high concentration region (area of the LDH islands). Hence, local domes would be formed on the polymer coatings.[70] The formed blister can eventually lead to local ruptures if the maximum elongation capacity of the polymer is exceeded, or, the blister continues to progress to the sides and delamination takes place. The effect of blistering has been discussed in investigations performed on LDH pigments incorporated into organic coatings.[40,66,71,72]

In addition to the above issues, the composition of the LDH synthesis bath can considerably influence the quality of the LDH conversion coating. Usually, the studies on the mechanism of corrosion of the IMCs in AA2024 are achieved in solution containing chloride salts. Chlorides are known to impair the Al native oxide layer and enhance the corrosion rate of the IMC and other Cu-based constituents composing the AA2024.[5–7,73,74] The corrosion acceleration factor provided by chlorides is absent in the current work, but instead nitrate and ammonium-based salts were used as precursors for the LDH synthesis. Ammonium-based salts were shown to exceptionally promote the dissolution of Cu.[75–78] Hypothetically, if ammonium ions come in contact with Cu from the IMC or detached Cu particles during dealloying, they can be driven to dissolution in the LDH bath and therefore may explain the strong dissolution rate shown in the AESEC profile. On the other hand, in the presence of nitrate ions, they are found to promote the passivation of Al alloys even in a chloride containing environment.[79] Nonetheless, nitrate ions not only act distinctly according to their concentration in the solution, but exercise a different effect on the Al matrix and the Cu-rich intermetallic. For instance, C. Blanc et al.[80] reported that when nitrates (NO$_3^-$) come in contact with Cu-rich IMC in AA2024, they are reduced to nitrite (NO$_2^-$) which in turn are reduced to form NH$_3$ (Eqs. 2–4).[80–82] The latter reacts with Cu ions to form soluble complexes, hence promoting the dissolution of the IMCs. The authors noted that the Al–Cu–Mg particles were the most impacted by the pitting due to nitrates, but the same phenomenon could happen on Al–Cu–Mn-Fe particles.[80] The increase of the local pH due to the successive reduction reaction (Eqs. 2–4) also favoured a strong dissolution of the adjacent Al matrix. However, the authors also noted that nitrates favour the growth of the Al oxide layer that is more protective on the

Al matrix than on the IMC.

$$O_2 + 2H_2O + 4e^- \rightleftharpoons 4OH^- \qquad [2]$$

$$NO_3^- + H_2O + 2e^- \rightleftharpoons NO_2^- + 2OH^- \qquad [3]$$

$$NO_2^- + 7H_2O + 6e^- \rightleftharpoons NH_3 + 2H_2O + 7OH^- \qquad [4]$$

The reduction of NO$_3^-$ to NH$_3$ was also the subject of the review from J. C. Fanning.[83] The author summarized a few conditions and factors that would favour this reduction process. It was stated that the reduction of NO$_3^-$ usually requires high temperature and pressure conditions in order to happen. However, they mentioned a few cases where Al in form of powder as an active metal to induce such reduction reactions at pH $\geqslant$ 10.5 and 50 °C–60 °C. These different studies around the mechanism of NO$_3^-$ to NH$_3$ still mean that it is a good hint to pursue but require a separate investigation.

A.C. Balaskas et al.[84] deduced in a comparative study of the corrosion inhibition of different nitrate-based salts on AA2024, that a high concentration of nitrate (15 mM) promotes Cu redeposition at cathodic sites, increasing the overall corrosion rate. Conversely, when comparing the inhibition effect of Ce salts (i.e. Ce(NO$_3$)$_3$, CeCl$_3$ and Ce(Ac)$_3$) on AA2024 and AA7075, P. Rodič et al.[85] noticed a passivation effect from nitrates, but Ce(NO$_3$)$_3$ still provided the weakest performance. If these assumptions are correct, this means that, on one hand we have a strong degradation of the Cu-based IMCs and significant dissolution of the Al matrix at the periphery of the IMC, and on the other hand, a stabilized passive film on the rest of the Al matrix. This could explain the strong inhomogeneous LDH layer observed in the current study.

In view of the current findings, to improve the formation of LDH conversion coatings on AA2024, is to envisage ways to minimise the dealloying process of the IMC while inducing a controlled destabilization of the native oxide layer to allow enough release of Al(OH)$_4^-$. Nitrate-based precursors have been systematically used for the LDH synthesis due to their very low affinity to LDH which allows possible intercalation of corrosion inhibitors but also the trapping of Cl$^-$ when used on their own.[66,86,87] These two factors are essential for the corrosion protection functionality of the LDH conversion coatings. Interlayer ions such as hydroxide (OH$^-$) and carbonates (CO$_3^{2-}$) make it very challenging to exploit the extrinsic self-healing functionality of the LDH coatings.[66] Therefore, it is important to investigate the effect of nitrate and ammonium ions on the degradation of the Cu-based IMC and ways to counteract it. For instance, instead of nitrate precursors, sodium salts precursors can be used. Additionally, it is possible to introduce a corrosion inhibitor directly during the synthesis (one pot procedure), as reported already in some works.[39,71,88–92] This could be reproduced for LDH conversion coatings as a way of minimising Cu-dealloying during the process of LDH production. Another way would be to explore other cation precursors for the hydroxide layers instead of Zn^{2+}. LiAl based LDH seem to produce a homogeneous layer on AA2024, as reported in early studies by Buchheit and colleagues[93–95] and more recently by P. Visser et al.[33,96] and A. Kosari et al.[69]

As a summary to the discussion above and taking into consideration what was learned from this study, a scheme of the main LDH growth stages on a Cu-rich IMC is illustrated in Fig. 11. The main processes can be summarised in 3 stages as following:

1) Initiation: This stage is characterized by the dissolution of the native oxide layer, the activation of the Cu-rich IMC and the beginning of the dealloying process. The role of ions such as ammonium in the dissolution of the Cu from the IMC will mainly manifest at the early stages of immersion.

2) Propagation: Further dealloying of the IMC and simultaneous growth of the LDH flakes above and on the surrounding of the IMC, with much developed LDH flakes on the border of the
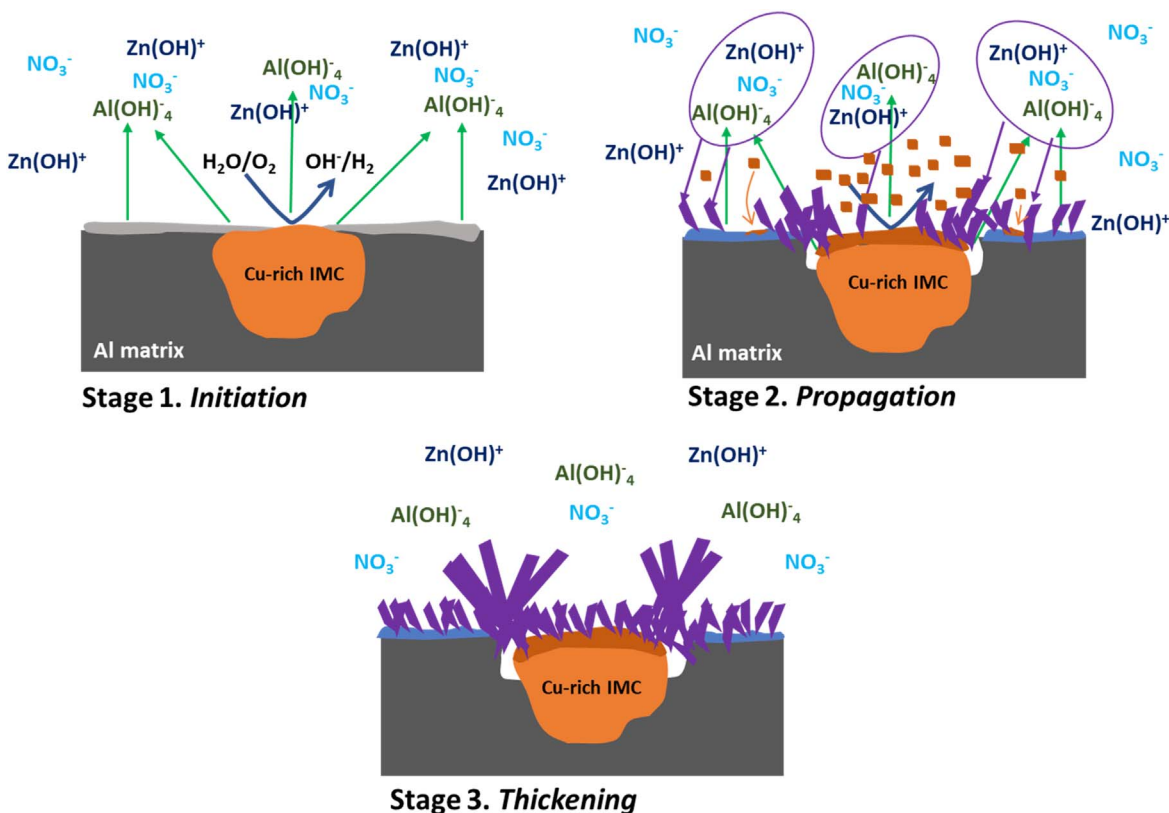
Figure 11. Generalized mechanism of LDH growth on a Cu-rich IMC in AA2024.

IMC. The latter is further triggered by the trenching process. Moreover, the growth of the LDH flakes does not immediately prevent the liberation of Cu clusters from the IMC as well as from the solid phase.

3) Thickening: At this point the effect of dealloying is strongly reduced due to the formation of a dense LDH layer above the Cu-rich intermetallic. A Cu-rich oxide layer is also formed above the IMC below the LDH conversion coating. Moreover, the borders of the IMC are covered with large and dense LDH islands, that hang above the lateral voids resulting from the trenching process.

Conclusions

This paper was devoted to the understanding of the influence of Cu-rich IMCs in the LDH conversion coating formation. A combination of various surface characterization methodologies was used to monitor the changes occurring at the area of the IMC. According to the AESEC and AFM/SKPFM results, the first minutes of immersion in the LDH synthesis bath are mainly characterized by an important dealloying and redeposition process. However, the simultaneous formation of the LDH flakes contributes to the slowing down of the dealloying process by the covering of the IMC. The SEM top view and cross section images indicate the establishment of an LDH film on top of the IMC after only 30 s of immersion.

The dealloying followed by the trenching of the IMCs leads to an excessive release of $Al(OH)_4^-$ which in turn leads to the formation of a denser LDH film in this region. However, the SEM cross-section images have shown that the dissolution of the Al matrix also leads to the creation of voids/cavities at the border of the IMCs. The LDH flakes do not form inside these cavities, hence they remain as empty defects that may weaken the protection properties of the LDH conversion coatings.

Another important factor that could be highlighted in the current study, is the role of the synthesis bath chemistry. Indeed, the source and composition of the starting precursors could have a significant influence on the homogeneity of the LDH growth. Nitrates and/or ammonium salts may enhance the corrosion of the IMCs while preserving the passivity of the rest of the Al matrix, which leads to an unbalance LDH growth mechanism and inhomogeneous coating formation. However, the methodologies used in the current work could not provide enough information on the mode of actions of these ions. These hypotheses need to be verified separately in future works.

Nevertheless, one of many advantages of LDH conversion coatings, is that they can be prepared through several pathways and be subjected to various pre- and post-treatment to optimize their performance. Therefore, it is possible to improve the quality of the LDH conversion coating by tuning the synthesis process.

ORCID

A. C. Bouali ⓘ https://orcid.org/0000-0003-0217-5747
M. Serdechnova ⓘ https://orcid.org/0000-0003-1879-5510
K.A. Yasakau ⓘ https://orcid.org/0000-0003-3596-1154
A. Lutz ⓘ https://orcid.org/0000-0003-0676-5170
H. Terryn ⓘ https://orcid.org/0000-0003-2639-5496
M.G.S. Ferreira ⓘ https://orcid.org/0000-0002-2071-9851
M.L. Zheludkevich ⓘ https://orcid.org/0000-0002-9658-9619

References

1. J. R. Davis, *Corrosion of Aluminum and Aluminum Alloys* (ASM International) (1999).
2. W. S. Miller, L. Zhuang, J. Bottema, A. J. Wittebrood, P. De Smet, A. Haszler, and A. Vieregge, "Recent development in aluminium alloys for the automotive industry." *Mat. Sci. Eng A.*, **280**, 37 (2000).
3. D. Varshney and K. Kumar, "Application and use of different aluminium alloys with respect to workability, strength and welding parameter optimization." *Ain Shams Eng. J.*, **12**, 1143 (2020).
4. T. Hashimoto, X. Zhang, X. Zhou, P. Skeldon, S. J. Haigh, and G. E. Thompson, "Investigation of dealloying of S phase (Al2CuMg) in AA 2024-T3 aluminium alloy using high resolution 2D and 3D electron imaging." *Corros. Sci.*, **103**, 157 (2016).
5. A. Boag, A. E. Hughes, A. M. Glenn, T. H. Muster, and D. McCulloch, "Corrosion of AA2024-T3 Part I: Localised corrosion of isolated IM particles." *Corros. Sci.*, **53**, 17 (2011).
6. A. E. Hughes, A. Boag, A. M. Glenn, D. McCulloch, T. H. Muster, C. Ryan, C. Luo, X. Zhou, and G. E. Thompson, "Corrosion of AA2024-T3 Part II: Co-operative corrosion." *Corros. Sci.*, **53**, 27 (2011).
7. A. M. Glenn, T. H. Muster, C. Luo, X. Zhou, G. E. Thompson, A. Boag, and A. E. Hughes, "Corrosion of AA2024-T3 part III: propagation." *Corros. Sci.*, **53**, 40 (2011).
8. M. Doerre, L. Hibbitts, G. Patrick, and N. K. Akafuah, "Advances in automotive conversion coatings during pretreatment of the body structure: A review." *Coatings.*, **8**, 420 (2018).
9. N. K. Akafuah, S. Poozesh, A. Salaimeh, G. Patrick, K. Lawler, and K. Saito, "Evolution of the automotive body coating process—A review." *Coatings.*, **6**, 24 (2016).
10. R. Twite and G. P. Bierwagen, "Review of alternatives to chromate for corrosion protection of aluminum aerospace alloys." *Prog. Org. Coat.*, **33**, 91 (1998).
11. A. E. Hughes, R. Taylor, and B. Hinton, "Chromate conversion coatings on 2024 Al alloy." *Surf. Interface Anal.*, **25**, 223 (1997).
12. M. S. Reisch, "Confronting the looming hexavalent chromium ban." *Chem. Eng. News*, **95**, 28–29 (2017).
13. P. Pokorny, P. Tej, and P. Szelag, "Chromate conversion coatings and their current application." *Metalurgija.*, **55**, 253 (2016).
14. G. S. Frankel and R. L. McCreery, "Inhibition of Al alloy corrosion by chromates." *Electrochem. Soc. Interface*, **10**, 34 (2001).
15. M. W. Kendig, A. J. Davenport, and H. S. Isaacs, "The mechanism of corrosion inhibition by chromate conversion coatings from X-ray absorption near edge spectroscopy (XANES)." *Corros. Sci.*, **34**, 41 (1993).
16. M. R. McGovern, P. Schmutz, R. G. Buchheit, and R. L. McCreery, "Formation of chromate conversion coatings on Al-Cu-Mg intermetallic compounds and alloys." *J. Electrochem. Soc.*, **147**, 4494 (2000).
17. M. Jaime Vasquez, G. P. Halada, C. R. Clayton, and J. P. Longtin, "On the nature of the chromate conversion coating formed on intermetallic constituents of AA2024-T3." *Surf. Interface Anal.*, **33**, 607 (2002).
18. J. Qi, A. Němcová, J. R. Walton, X. Zhou, P. Skeldon, and G. E. Thompsona, "Influence of pre-and post-treatments on formation of a trivalent chromium conversion coating on AA2024 alloy." *Thin Solid Films*, **616**, 270 (2016).
19. J. T. Qi, T. Hashimoto, J. R. Walton, X. Zhou, P. Skeldon, and G. E. Thompson, "Trivalent chromium conversion coating formation on aluminium." *Surf. Coat. Technol.*, **280**, 317 (2015).
20. R. Saillard, B. Viguier, G. Odemer, A. Pugliara, B. Fori, and C. Blanc, "Influence of the microstructure on the corrosion behaviour of 2024 aluminium alloy coated with a trivalent chromium conversion layer." *Corros. Sci.*, **142**, 119 (2018).
21. P. Campestrini, H. Terryn, A. Hovestad, and J. H. W. De Wit, "Formation of a cerium-based conversion coating on AA2024: relationship with the microstructure." *Surf. Coat. Technol.*, **176**, 365 (2004).
22. S. Sainis, S. Roșoiu, E. Ghassemali, and C. Zanella, "The role of microstructure and cathodic intermetallics in localised deposition mechanism of conversion compounds on Al (Si, Fe, Cu) alloy." *Surf. Coat. Technol.*, **402**, 126502 (2020).
23. I. Milošev and G. S. Frankel, "Conversion coatings based on zirconium and/or titanium." *J. Electrochem. Soc.*, **165**, C127 (2018).
24. L. Li, B. W. Whitman, and G. M. Swain, "Characterization and performance of a Zr/Ti pretreatment conversion coating on AA2024-T3." *J. Electrochem. Soc.*, **162**, C279 (2015).
25. L. Li, B. W. Whitman, C. A. Munson, R. Estrada, C. A. Matzdorf, and G. M. Swain, "Structure and corrosion performance of a non-chromium process (NCP) Zr/Zn pretreatment conversion coating on aluminum alloys." *J. Electrochem. Soc.*, **163**, C718 (2016).

26. N. Iyi, Y. Ebina, and T. Sasaki, "Water-swellable MgAl− LDH (layered double hydroxide) hybrids: synthesis, characterization, and film preparation." *Langmuir*, **24**, 5591 (2008).
27. J. Tedim, M. L. Zheludkevich, A. N. Salak, A. Lisenkov, and M. G. S. Ferreira, "Nanostructured LDH-container layer with active protection functionality." *J. Mater. Chem.*, **21**, 15464 (2011).
28. J. Tedim, M. L. Zheludkevich, A. C. Bastos, A. N. Salak, J. Carneiro, F. Maia, A. D. Lisenkov, A. B. Oliveira, and M. G. S. Ferreira, "Effect of surface treatment on the performance of LDH conversion films." *ECS Electrochem. Lett.*, **3**, C4 (2014).
29. J. Tedim, A. C. Bastos, S. Kallip, M. L. Zheludkevich, and M. G. S. Ferreira, "Corrosion protection of AA2024-T3 by LDH conversion films. Analysis of SVET results." *Electrochim. Acta*, **210**, 215 (2016).
30. K. A. Yasakau, A. Kuznetsova, S. Kallip, M. Starykevich, J. Tedim, M. G. S. Ferreira, and M. L. Zheludkevich, "A novel bilayer system comprising LDH conversion layer and sol-gel coating for active corrosion protection of AA2024." *Corros. Sci.*, **143**, 299 (2018).
31. B. Kuznetsov, M. Serdechnova, J. Tedim, M. Starykevich, S. Kallip, M. P. Oliveira, T. Hack, S. Nixon, M. G. S. Ferreira, and M. L. Zheludkevich, "Sealing of tartaric sulfuric (TSA) anodized AA2024 with nanostructured LDH layers." *RSC Adv.*, **6**, 13942 (2016).
32. M. Serdechnova, M. Mohedano, B. Kuznetsov, C. L. Mendis, M. Starykevich, S. Karpushenkov, J. Tedim, M. G. S. Ferreira, C. Blawert, and M. L. Zheludkevich, "PEO coatings with active protection based on in situ formed LDH-nanocontainers." *J. Electrochem. Soc.*, **164**, C36 (2016).
33. P. Visser, Y. Gonzalez-Garcia, J. M. Mol, and H. Terryn, "Mechanism of passive layer formation on AA2024-T3 from alkaline lithium carbonate solutions in the presence of sodium chloride." *J. Electrochem. Soc.*, **165**, C60 (2018).
34. R. G. Buchheit, R. P. Grant, P. F. Hlava, B. Mckenzie, and G. L. Zender, "Local dissolution phenomena associated with S phase (Al2CuMg) particles in aluminum alloy 2024-T3." *J. Electrochem. Soc.*, **144**, 2621 (1997).
35. Y. Wang, Y. Zhang, B. Zhou, C. Li, F. Gao, X. Wang, D. Liang, and Y. Wei, "In-situ observation of the growth behavior of ZnAl layered double hydroxide film using EQCM." *Mater. Des.*, **180**, 107952 (2019).
36. A. C. Bouali et al., "Mechanism of LDH direct growth on aluminum alloy surface: a kinetic and morphological approach." *J. Phys. Chem. C*, **125**, 11687 (2021).
37. M. Serdechnova, P. Volovitch, and K. Ogle, "Atomic emission spectroelectro-chemistry study of the degradation mechanism of model high-temperature paint containing sacrificial aluminum particles." *Surf. Coat. Technol.*, **206**, 2133 (2012).
38. A. C. Tedim et al., "LDH growth on AA2024 and zinc and their intercalation with chloride: Comparison of crystal structure and kinetics." *Appl. Surf. Sci.*, **501**, 144027 (2020).
39. M. A. Iqbal, L. Sun, A. T. Barrett, and M. Fedel, "Layered double hydroxide protective films developed on aluminum and aluminum alloys: synthetic methods and anti-corrosion mechanisms." *Coatings.*, **10**, 428 (2020).
40. M. L. Zheludkevich, S. K. Poznyak, L. M. Rodrigues, D. Raps, T. Hack, L. F. Dick, T. Nunes, and M. G. S. Ferreira, "Active protection coatings with layered double hydroxide nanocontainers of corrosion inhibitor." *Corros. Sci.*, **52**, 602 (2010).
41. P. Schmutz and G. S. Frankel, "Characterization of AA2024-T3 by scanning kelvin probe force microscopy." *J. Electrochem. Soc.*, **145**, 2285 (1998).
42. K. A. Yasakau, M. L. Zheludkevich, S. V. Lamaka, and M. G. S. Ferreira, "Mechanism of corrosion inhibition of AA2024 by rare-earth compounds." *J. Phys. Chem. B*, **110**, 5515 (2006).
43. A. K. Yasakau, A. N. Salak, M. L. Zheludkevich, and M. G. S. Ferreira, "Volta potential of oxidized aluminum studied by scanning Kelvin probe force microscopy." *J. Phy. Chem. C.*, **114**, 8474 (2010).
44. J. T. Kloprogge, L. Hickey, and R. L. Frost, "FT-Raman and FT-IR spectroscopic study of synthetic Mg/Zn/Al-hydrotalcites." *J. Raman Spectrosc.*, **35**, 967 (2004).
45. J. T. Kloprogge, D. Wharton, L. Hickey, and R. L. Frost, "Infrared and Raman study of interlayer anions CO32−, NO3−, SO42− and ClO4− in Mg/Al-hydrotalcite." *Am. Min.*, **87**, 623 (2002).
46. I. D. Dobrea, C. E. Ciocan, E. Dumitriu, M. I. Popa, E. Petit, and V. Hulea, "Raman spectroscopy—Useful tool for studying the catalysts derived from Mo and V-oxyanion-intercalated layered double hydroxides." *Appl. Clay Sci.*, **104**, 205 (2015).
47. A. Ianoul, T. Coleman, and S. A. Asher, "UV resonance Raman spectroscopic detection of nitrate and nitrite in wastewater treatment processes." *Anal. Chem.*, **74**, 1458 (2002).
48. M. D. Fontana, K. B. Mabrouk, and T. Kauffmann, *Raman Probe of pollutants in water: Measurement process. 4th Imeko TC19 Symposium on Environmental Instrumentation and Measurements Protecting Environment, Climate Changes and Pollution Control. IMEKO Budapest, Hungary* (2013).
49. M. R. Islam, Z. Guo, D. Rutman, and T. J. Benson, "Immobilization of triazabicyclodecene in surfactant modified Mg/Al layered double hydroxides." *RSC Adv.*, **3**, 24247 (2013).
50. M. Rashad, M. Rüsing, G. Berth, K. Lischka, and A. Pawlis, "CuO and Co3O4 nanoparticles: synthesis, characterizations, and Raman spectroscopy." *J. Nanomater.*, **2013**, 82 (2013).
51. M. R. Joya, J. Barba, and A. Raba, "Vibrational Raman modes and particle size analysis of cupric oxide with calcination temperature." *J. Pure Appl. Phys.*, **57**, 268 (2019).
52. T. H. Tran and V. T. Nguyen, "Copper oxide nanomaterials prepared by solution methods, some properties, and potential applications: a brief review." *Int. Sch. Res. Notices.*, **2014**, 1 (2014).
53. A. Gergely, "A review on corrosion protection with single-layer, multilayer, and composites of graphene." *Corros. Rev.*, **36**, 155 (2018).

54. S. Chakraborty, A. Das, M. R. Begum, S. Dhara, and A. K. Tyagi, "Vibrational properties of CuO nanoparticles synthesized by hydrothermal technique." *AIP Conference Proceedings* (American Institute of Physics, Geneva, Switzerland) 1349, 841 (2011).

55. P. M. Castro and P. W. Jagodzinski, "FTIR and Raman spectra and structure of Cu (NO3)+ in aqueous solution and acetone." *Spectrochim. Acta A*, **47**, 1707 (1991).

56. G. Kalita, M. E. Ayhan, S. Sharma, S. M. Shinde, D. Ghimire, K. Wakita, M. Umeno, and M. Tanemura, "Low temperature deposited graphene by surface wave plasma CVD as effective oxidation resistive barrier." *Corros. Sci.*, **78**, 183 (2014).

57. K. Ogle, "Atomic emission spectroelectrochemistry: real-time rate measurements of dissolution, corrosion, and passivation." *Corrosion*, **75**, 1398 (2019).

58. N. Dimitrov, J. A. Mann, M. Vukmirovic, and K. Sieradzki, "Dealloying of Al2CuMg." *in alkaline media, J. Electrochem. Soc.*, **147**, 3283 (2000).

59. M. Vukmirovic, N. Dimitrov, and K. Sieradzki, "Dealloying and corrosion of Al alloy 2024 T3." *J. Electrocham. Soc.*, **149**, B428 (2002).

60. A. Kosari, H. Zandbergen, F. Tichelaar, P. Visser, P. Taheri, H. Terryn, and J. M. C. Mol, "In-situ nanoscopic observations of dealloying-driven local corrosion from surface initiation to in-depth propagation." *Corros. Sci.*, **177**, 108912 (2020).

61. A. Kosari, F. Tichelaar, P. Visser, H. Zandbergen, H. Terryn, and J. M. C. Mol, "Dealloying-driven local corrosion by intermetallic constituent particles and dispersoids in aerospace aluminium alloys." *Corros. Sci.*, **177**, 108947 (2020).

62. M. Olgiati, P. J. Denissen, and S. J. Garcia, "When all intermetallics dealloy in AA2024-T3: Quantifying early stage intermetallic corrosion kinetics under immersion." *Corros. Sci.*, **192**, 109836 (2021).

63. N. Birbilis and R. G. Buchheit, "Electrochemical characteristics of intermetallic phases in aluminum alloys: an experimental survey and discussion." *J. Electrochem. Soc.*, **152**, B140 (2005).

64. Y.-X. Zhu, G. L.S., D.-J. Zheng, M. Serdechnova, C. Blawert, and M. L. Zheludkevich, "In situ synergistic strategy of sacrificial intermedium for scalable-manufactured and controllable layered double hydroxide film." *Sci. China Mater.*, **65**, 1 (2022).

65. M. Mokaddem, P. Volovitch, F. Rechou, R. Oltra, and K. Ogle, "The anodic and cathodic dissolution of Al and Al–Cu–Mg alloy." *Electrochim. Acta*, **55**, 3779 (2010).

66. A. C. Bouali, M. Serdechnova, C. Blawert, J. Tedim, M. G. S. Ferreira, and M. L. Zheludkevich, "Layered double hydroxides (LDHs) as functional materials for the corrosion protection of aluminum alloys: A review." *Appl. Mat. Today.*, **21**, 100857 (2020).

67. F. Zhang, C. L. Zhang, S. Liang, R. C. Zeng, Z. G. Liu, and H. Z. Cui, "Corrosion of in situ grown MgAl-LDH coating on aluminum alloy." *Trans. Nonferrous Met. Soc. China*, **25**, 3498 (2015).

68. L. Wang, Q. Zong, W. Sun, Z. Yang, and G. Liu, "Chemical modification of hydrotalcite coating for enhanced corrosion resistance." *Corros. Sci.*, **93**, 256 (2015).

69. A. Kosari, F. Tichelaar, P. Visser, H. Zandbergen, H. Terryn, and J. M. C. Mol, "Laterally-resolved formation mechanism of a lithium-based conversion layer at the matrix and intermetallic particles in aerospace aluminium alloys." *Corros. Sci.*, **190**, 109651 (2021).

70. S. Effendy, T. Zhou, H. Eichman, M. Petr, and M. Z. Bazant, "Blistering failure of elastic coatings with applications to corrosion resistance." *Soft Matter.*, **17**, 9480 (2021).

71. J. M. Vega, N. Granizo, D. De La Fuente, J. Simancas, and M. Morcillo, "Corrosion inhibition of aluminum by coatings formulated with Al–Zn–vanadate hydrotalcite." *Prog. Org. Coat.*, **70**, 213 (2021).

72. S. Mahajanam and R. G. Buchheit, "Characterization of Zn-Al-V 10 O 28 6− corrosion-inhibiting hydrotalcite pigments in epoxy resins." *corrosion*, **64**, 230–240 (2004).

73. F. M. Queiroz, M. Magnani, I. Costa, and H. G. De Melo, "Investigation of the corrosion behaviour of AA 2024-T3 in low concentrated chloride media." *Corros. Sci.*, **50**, 2646 (2008).

74. B. N. Grgur and L. Marunkić, "The influence of chloride anions on the pitting corrosion of aluminum alloy EN 46000." *Zaštita materijala.*, **59**, 243 (2018).

75. Q. Luo, R. Mackay, and S. Babu, "Copper dissolution in aqueous ammonia-containing media during chemical mechanical polishing." *Chem. Mater.*, **9**, 2101 (1997).

76. V. Radmehr, S. M. J. Koleini, M. R. Khalesi, and M. R. Tavakoli, "Ammonia leaching in the copper industry: a review." *XXVI international mineral processing congress (IMPC) proceedings/New Delhi, India/24–28 September*, pp. 02512 (2012).

77. A. R. Johnson, T. M. McQueen, and K. T. Rodolfa, "Species distribution diagrams in the copper-ammonia system: An updated and expanded demonstration illustrating complex equilibria." *J. Chem. Educ.*, **82**, 02512 (2005).

78. D. Strmčnik, M. Gaberšček, B. Pihlar, D. Kočar, and J. Jamnik, "Copper dissolution in ammonia solutions: identification of the mechanism at low overpotentials." *J. Electrochem. Soc.*, **156**, C222 (2009).

79. M. Starostin, G. Shter, and G. Grader, "Corrosion of aluminum alloys Al 6061 and Al 2024 in ammonium nitrate-urea solution." *Corros. Mater.*, **67**, 387 (2016).

80. C. Blanc, S. Gastaud, and G. Mankowski, "Mechanistic studies of the corrosion of 2024 aluminum alloy in nitrate solutions." *J. Electrochem. Soc.*, **150**, B396 (2003).

81. A. Adams, K. Eagle, and R. Foley, "Synergistic effects of anions in the corrosion of aluminum alloys." *J. Electochem. Soc.*, **119**, 1692 (1972).

82. E. Filimonov and A. Shcherbakov, "Catalytic effect of copper ions on nitrate reduction." *Prot. Met.*, **40**, 280 (2004).

83. J. C. Fanning, "The chemical reduction of nitrate in aqueous solution." *Coord. Chem. Rev.*, **199**, 159 (2000).

84. A. C. Balaskas, I. A. Kartsonakis, L. A. Tziveleka, and G. C. Kordas, "Improvement of anti-corrosive properties of epoxy-coated AA 2024-T3 with TiO2 nanocontainers loaded with 8-hydroxyquinoline." *Prog. Org. Coat.*, **74**, 418 (2012).

85. P. Rodič and I. Milošev, "Corrosion inhibition of pure aluminium and alloys AA2024-T3 and AA7075-T6 by cerium (III) and cerium (IV) salts." *J. Electrochem. Soc.*, **163**, C85 (2016).

86. S. Miyata, "Anion-exchange properties of hydrotalcite-like compounds." *Clays Clay Miner.*, **31**, 305 (1983).

87. D. G. Costa, A. B. Rocha, W. F. Souza, S. S. X. Chiaro, and A. A. Leitão, "Comparative Structural, thermodynamic and electronic analyses of ZnAlAn− hydrotalcite-like compounds (An− Cl−, F−, Br−, OH−, CO32− or NO3−): An *ab initio* study." *Appl. Clay Sci.*, **56**, 16 (2012).

88. S. Mahajanam and R. G. Buchheit, "Characterization of inhibitor release from Zn-Al-[V10O28]6− hydrotalcite pigments and corrosion protection from hydrotalcite-pigmented epoxy coatings." *Corrosion*, **64**, 230 (2008).

89. R. G. Buchheit, H. Guan, S. Mahajanam, and F. Wong, "Active corrosion protection and corrosion sensing in chromate-free organic coatings." *Prog. Org. Coat.*, **47**, 174 (2003).

90. M. J. Anjum, J. Zhao, V. Z. Asl, G. Yasin, W. Wang, S. Wei, Z. Zhao, and W. Q. Khan, "In-situ intercalation of 8-hydroxyquinoline in Mg-Al LDH coating to improve the corrosion resistance of AZ31." *Corros. Sci.*, **157**, 1 (2019).

91. T. Hu, Y. Ouyang, Z. H. Xie, and L. Wu, "One-pot scalable in situ growth of highly corrosion-resistant MgAl-LDH/MBT composite coating on magnesium alloy under mild conditions." *J. Mater. Sci. Technol.*, **92**, 225 (2021).

92. R. C. Zeng, Z. G. Liu, F. Zhang, S. Q. Li, H. Z. Cui, and E. H. Han, "Corrosion of molybdate intercalated hydrotalcite coating on AZ31 Mg alloy." *J. Mater. Chem. A*, **2**, 13049 (2014).

93. R. G. Buchheit, M. Bode, and G. J. C. Stoner, "Corrosion-resistant, chromate-free talc coatings for aluminum." *Corrosion*, **50**, 205 (1994).

94. R. B. Leggat, W. Zhang, R. G. Buchheit, and S. R. Taylor, "Performance of hydrotalcite conversion treatments on AA2024-T3 when used in a coating system." *Corrosion*, **58**, 322 (2002).

95. W. Zhang and R. J. C. Buchheit, "Hydrotalcite coating formation on Al-Cu-Mg alloys from oxidizing bath chemistries." *Corrosion*, **58**, 591 (2002).

96. P. Visser, Y. Liu, H. Terryn, and J. C. M. Mol, "Lithium salts as leachable corrosion inhibitors and potential replacement for hexavalent chromium in organic coatings for the protection of aluminum alloys." *J. Coat. Technol. Res.*, **13**, 557 (2016).